Science
AAAS

Supplementary Materials for

Dynamics of particle network in composite battery cathodes

Jizhou Li *et al*.

Corresponding authors: Feng Lin, fenglin@vt.edu; Kejie Zhao, kjzhao@purdue.edu; Yijin Liu, liuyijin@slac.stanford.edu

Science **376**, 517 (2022)
DOI: 10.1126/science.abm8962

The PDF file includes:

Materials and Methods

Composite electrode preparation

The composite cathodes were prepared by spreading the slurry (N-methyl-2-pyrrolidone as the solvent) with active materials (90 wt%), acetylene carbon (5 wt%), and polyvinylidene difluoride (5 wt%) as the binder and casting them on carbon-coated aluminum foils. The electrodes were then dried overnight at 120 °C in a vacuum oven and transferred into an Ar-filled glove box for future use. The areal active mass loading is around 8.0 mg/cm^2. The volume fractions of active particles, the liquid electrolyte, and the carbon-binder matrix are about 40%, 30%, and 30%, respectively. It resulted in the porosity of the homogenized matrix being 0.5. This relatively high porosity is because the electrode was not calendered to avoid any pre-damage caused by the calendering process. Note that the electrode with lower porosity could also lead to insufficient/inhomogeneous electrolyte wetting, which induces chemical inhomogeneity through a different mechanism. In this work, we focus on NMC particle's intrinsic behavior during battery operation and, therefore, we choose well-formed electrode without the calendering process as our model system. We believe that our findings and interpretation are fundamental and can be applicable to the design of real-world batteries. The electrochemical cycling of these electrodes followed the same procedure as what was reported previously (*1*, *28*). Specifically, CR2032-type coin cells were assembled in an Argon filled glovebox (typical H_2O <0.1 ppm, O_2 <0.1 ppm) with the composite cathode. Glass fiber separator (Whatman), Li metal anode, and 1 M $LiPF_6$ dissolved in a 3:7 weight ratio of ethylene carbonate/ethyl methyl carbonate with 2 wt% vinylene carbonate electrolytes were used for the coin cells. All the coin cells went through a formation cycle at 0.1C between 2.5-4.5 V. After the formation cycle, the coin cells were cycled at 5C between 2.5-4.5 V for 10 cycles or 50 cycles, respectively. The coin cells were rested for 2 minutes between the charge and discharge reactions. The electrochemical performance of these coin cells is included in **Fig. S1**. 1C was defined as fully charging the composite cathode in 1h with a specific capacity of 200 mAh g^{-1}. All the voltage in this manuscript was defined as against Li^+/Li. The tomography scan was conducted near the center of the piece, away from the cut edges to avoid any sample prep induced artifacts. All the samples were protected in the inert gas environment during storage, transportation, handling, and measurements.

X-ray phase contrast holo-tomography

The X-ray phase contrast nano tomography experiments were conducted at the ID16A-NI nano-imaging beamline at the European Synchrotron Radiation Facility (ESRF) in Grenoble, France. This beamline features a high energy hard X-ray nano-probe (*44*), delivering a focus down to ~20 nm with a brilliant photon flux (up to 10^{12} photons/s at $\Delta E/E \sim 1\%$). The nano-focus is achieved by two pairs of multilayer-coated Kirkpatrick–Baez (KB) optics, working at 17 and 33.6 keV, respectively. This experiment was taken under 17 keV. For every tomography scan, 1500 projections were acquired with 0.2s exposure time. One complete phase contrast nano-tomography scan constitutes tomograms at four different focus-to-sample distances. These tomograms were subsequently used for phase retrieval to generate 2D phase maps (*45*). The 2D phase maps retrieved from all angular projections were then used as input for a tomographic reconstruction based on the filtered back projection algorithm method (ESRF PyHST2 software package (*46*), http://ftp.esrf.fr/scisoft/PYHST2).

Morphology-informed neural network for 3D particle identification

We extend our previous work on successfully identifying the $LiNi_{0.8}Mn_{0.1}Co_{0.1}O_2$ (NMC) particles on monolayer electrode using the convolutional neural network (CNN) (*1*) by considering the morphology of those NMC particles based on the StarDist network (*47*) to improve the identification accuracy. Moreover, we propose here a fusion strategy to extend the pretrained 2D model without requiring 3D-labeled data. The input volume is resliced into three different sections (xy, yz and xz). Then the outputs from all sections are fused together to obtain the final 3D segmentation (see **Fig. S2**).

Specifically, the shape of each NMC particle is modeled as a star-convex polygon (*47*). A convolutional neural network with U-Net architecture (*48*) is used to densely predict the representation and a value that indicates the possibilities of one particle. For each pixel (x, y) with index i, j, the CNN is trained to regress the radial distances $d_k(x, y)$ $(k = 1, \dots, n)$ to the object boundary and additionally a particle probability $p(x, y)$ defined as the normalized Euclidean distance to the nearest background pixels. n represents the number of rays to describe the shape of the polygon, which is set as 32 to achieve a sufficiently accuracy. During the training, we use a loss function $\mathcal{L}_{loss} = \mathcal{L}_{obj} + \lambda \mathcal{L}_{dist}$ which combining a binary cross-entropy function $\mathcal{L}_{obj}$ and mean absolute error $\mathcal{L}_{dist}$ over all pixels. The parameter λ is tuned as 0.2 to get the best performance. After the prediction by CNN, the non-maximum suppression (NMS) is adopted to get only one shape for every particle in the image (*47*). The particle shapes are further refined by removing pixels that were predicted by the neural network to be outside of particles through simple intensity thresholding. We train the neural network using 322 images with their ground truth 2D labels, in which 90% of the images are used for training and 10% for validation. Images are augmented via axis-aligned rotations and flips. The network architecture details and comparison of different methods on typical images are shown in **Fig. S3.** Note that comparing with the traditional watershed algorithm and our previous method (*1*), the method present in this work shows significantly improved robustness against the formation of the inner-particle cracks, as well as the distinguishability of closely located particles.

It is worth noting that there are still challenging cases where some regions are missed in single 2D images (e.g. the xy section) due to various factors such as the low contrast and tomography reconstruction artifacts. However, the missing information is often available in other sections, for example the xz and yz views. This observation motivates us to construct a new intermediate representation of a particle by fusing labels from different sections. To elucidate this redundancy, the predicted 2D particle probability maps from xy, yz and xz sections are averaged together followed by a clustering of pixels that essentially converge to the particle labels with connected components. This procedure ensures that all the particles can be accurately identified and quantified, which was manually inspected and refined.

This approach integrated the morphological information of NMC particles into the neural network and generalized the pre-trained 2D model to 3D particle identification. It helps to increase the segmentation sensitivity and avoids the computation and memory issues for 3D segmentation network by running the neural networks on every 2D section. We should point out that, this approach is particularly suitable for the highly accurate identification of NMC particles on the tomography data of multi-layer electrode, in which the previous method (*1*) designed for single layer electrode fails due to a lack of expressive power such as an inability of precisely follow particle boundaries in different slices or to incorporate information from different sections. In

addition, although most of particles considered in this work are with roughly spherical shape, the morphology-informed neural network (*47*) can be applied to other particle shapes as well, for instance the single-crystal cathode.

Finite element analysis

We perform finite element analysis to understand the evolution of electrochemical activity and mechanical damage during (dis)charge cycles. The geometry for the half cell consists of a cathode current collector at the bottom, carbon/binder (CB) domains enclosing the NMC active particles (10 μm diameter), a separator, and a Li metal at the top. Galvanostatic charging and discharging occur at a 5C rate. The CB domain is porous (50%) and is filled with the electrolyte. The CB domain only conducts electrons and does not transport Li-ions. The electrolyte transports Li-ions in both the CB and the separator regions. The governing equations of the electro-chemo-mechanics model, including electron conduction in the CB domain, Li transport in the liquid electrolyte across the porous composite electrode, charge transfer at the interface between the NMC particles and the electrolyte, Li diffusion within the NMC particles, and mechanical deformation and stresses in NMC and CB, are the same as described in detail in our prior publication (*3*). Within NMC particles, the gradients of both concentration and hydrostatic stress contribute towards the flux. The isotropic diffusivity of NMC is $D = 2 \times 10^{-14}$ m^2/s. The electrical conductivity of the high conductivity CB domain is 100 S/m, and the value for low conductivity CB is 2×10^{-3} S/m. A zero-displacement boundary condition is prescribed at the outer edges of the CB domain.

The stress field is calculated using the mechanical equilibrium equation, $\nabla \cdot \boldsymbol{\sigma} = 0$. The stress-strain relation follows Hook's law, $\boldsymbol{\sigma} = \mathbf{C}\text{:}\, \boldsymbol{\varepsilon_{el}}$, where $\mathbf{C}$ is the elastic stiffness matrix and $\boldsymbol{\varepsilon_{el}}$ is the elastic strain matrix. The NMC (E = 140 GPa, ν = 0.3) and CB (E = 2 GPa, ν = 0.3) are modeled as linearly elastic isotropic materials, E is the elastic modulus and ν is the Poisson's ratio. We assume a linearly isotropic volumetric change with the variation of lithium concentration, $\boldsymbol{\varepsilon_{Li}} = (1/3)\Omega_V(C - C_{ini})\mathbf{I}$, where $\boldsymbol{\varepsilon_{Li}}$ is the lithiation induced strain, Ω_V is the partial molar volume of Li atom, C is the Li concentration and C_{ini} is the initial Li concentration at the stress-free state. The cohesive bi-linear traction-separation curve determines the damage at the interface of NMC active particles and CB. The tensile strength for the cohesive zone is 300 MPa, and the fracture energy is 0.4 J/m^2.

The modified Butler Volmer kinetics is $\eta = \phi_s - \phi_l - E_{eq} - (i_{BV} \cdot R)$, where η is the driving overpotential, ϕ_s is electric potential, ϕ_l is electrolyte potential, E_{eq} is equilibrium potential, i_{BV} is current through the interface, R is the resistance term and $(i_{BV} \cdot R)$ represents the correction in driving force due to the damage-induced electrical contact loss. The resistance term is defined as $R = R_0 e^{(\lambda+\lambda_{ini})/\lambda_{ref}}$, where $R_0 = 1.0 \times 10^{-3}\ \Omega \cdot \text{m}^2$, λ is the gap at the NMC and CB interface, $\lambda_{ini} = 0$ for high conductivity CB and $\lambda_{ini} = 0.2$ nm for low conductivity CB and $\lambda_{ref} = 1$ nm. The other parameters used for the computational modeling are listed in the Table 1 in the previous publication (*3*). The governing equations of diffusion kinetics and deformation kinematics are solved simultaneously at every time step in COMSOL Multiphysics. We use built-in time-dependent solver MUMPS (MUltifrontal Massively Parallel sparse direct Solver) to solve the evolution of lithium concentration, stress field, and damage.

Regularized auto-encoder network for dimensionality reduction

We firstly feed the extracted attributes into the regularized autoencoder neural network. The purpose of this step is to reduce the dimensionality of the attribute space while retaining the most valuable information. Importantly, the relationship between attributes embedded in the original space is rather non-linear.

The autoencoder network is composed of an encoder, a latent representation and a decoder (*31*). The encoder is to compress the data to their low-dimensional representation and the decoder tries to reconstruct the latent representation back to their initial dimension. The purpose of training an autoencoder is to minimize the reconstruction loss while removing the noise in the input data as much as possible. In this work, we incorporate the sparsity regularization and ℓ_2 regularization to prevent autoencoder from learning identity function and to improve their ability to capture important information and obtain richer representation. A schematic illustration of the network architecture is shown in **Fig. S8A.**

Specifically, the loss function for training the autoencoder network is defined as follows:

$$\mathcal{L}_{AE} = \frac{1}{n}||\mathrm{Y} - \hat{Y}||_2^2 + \lambda\mathcal{R}_{\ell_2} + \beta\mathcal{R}_{\text{sparsity}},$$

where n is the number of input data Y, $\hat{\mathrm{Y}}$ is the reconstructed data with reduced noise and enhanced correlation among attributes. $\mathcal{R}_{\ell_2}$ and $\mathcal{R}_{\text{sparsity}}$ are the ℓ_2 and sparsity regularizer, respectively. λ and β are the corresponding regularization parameters, which are set to be 0.001 and 0.01 respectively. We choose the number of latent representations to be 9 using cross-validation on the validation set (5%) to minimize the validation error (**Fig. S8B**). The advantage of the adopted regularization strategies regarding better coding-decoding performance is demonstrated in **Figs. S8C and S8D**.

The correlations of the latent representations and reconstructed attributes are calculated by the Pearson correlation coefficient. They are subsequently visualized by the Circular plots (*34*). A useful property of the autoencoder network is that it not only provides low-dimensional representations by learning important attributes but also allows reconstructing back to the original space. By sorting the LDs based on their respective significance and selectively removing the unimportant LDs prior to decoding, the coding-decoding process could suppress the effects of noise in the experimental data and uncertainties in the attribute extraction. This is particularly important for our application because the correlations among different LDs contain rich information but without offering specific physical justification and implications. Thus we further compose the circular correlation maps among the top-15-ranked original attributes for the datasets of 10-cycled and 50-cycled electrodes, respectively (**Fig. S10**). A quick assessment of the difference between 10-cycled and 50-cycled data suggests that some attributes seem to play a different role at a later stage of the battery operation. However, this one-to-one Pearson correlation could potentially induce the misinterpretation of variables due to its limited robustness in handling the highly complicated multivariable systems, which motivates the subsequent regression analysis.

Random forest regression and identification of contribution scores

We utilize the random forest (RF) regression (*32*), which is one of the most popular tree-based ensemble-learning methods, for the regression of the damage degrees with respect to the other attributes of all particles in a supervised manner. It operates by constructing a multitude of decision

trees in the training process and outputting the mean prediction of the individual trees. We split the data into training and test datasets (95% / 5%) and quantify the regression performance using mean absolute error (MAE) which is defined as $MAE = \frac{1}{T}\sum_{t=1}^{T}|A_t - P_t|$, where A_t is the actual value of the particle damage and P_t is the fitted value. The maximum depth of the random forest tree is set to be 30.

The SHAP (SHapley Additive exPlanations) (*33*) is used to tell how to rank the attribute importance of the particle properties to the damage level. SHAP values are computed in a way that attempts to isolate away of correlation and interaction as well. Attributes with large absolute Shapley values (*37*) are considered to be important. The global importance is obtained from the summation of the absolute Shapley values per attribute across the data. To diminish the spurious contributions coming from the algorithm initialization and data size, we trained various regression models through two robustness validation strategies (denoted by scattering dots with triangle and square markers in **Fig. 4** respectively): 1) instead of using the full training data, we randomly draw 500 particles for 10 times and performed the regression; 2) the randomness of the bootstrapping of the samples used when building trees and the sampling of the attributes to consider when looking for the best split at each node are set to be 10 different values. The consistency among different models, along with the usage of cross-validation when testing, allows us to better interpret the models with robustness demonstration and reliability.

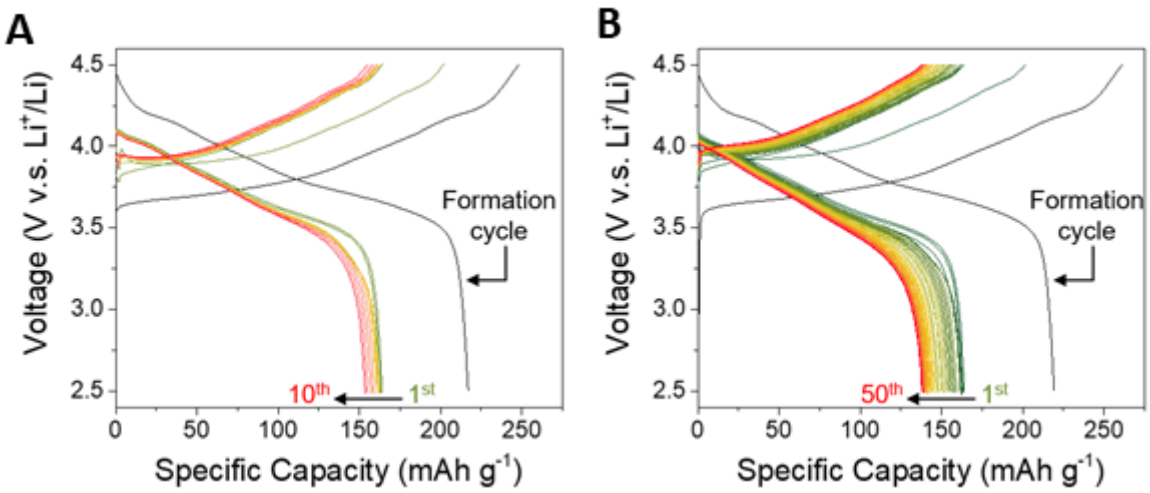

Fig. S1. **The Electrochemical performance of the coin cells used in this study.** All the coin cells went through a formation cycle at 0.1C. After the formation cycle, the coin cells were cycled at 5C for (a) 10 cycles or (b) 50 cycles. The voltage curves of the coin cells are color-coded, with the initial cycles in green and the end cycles in red. All the coin cells were cycled between 2.5-4.5 V.

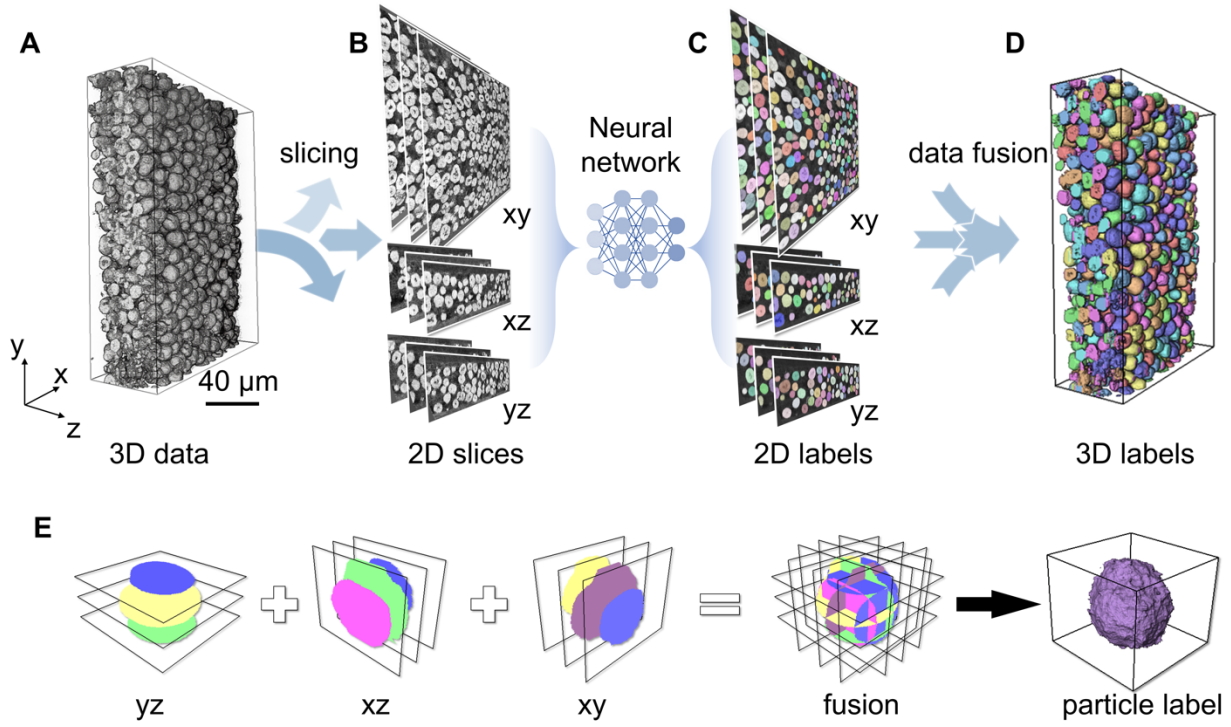

Fig. S2. Illustration of the 3D particle identification method. (**A**) The input 3D tomography data is firstly sliced into three sections by slicing in different directions. (**B-C**) Each 2D section is passed through the morphology-informed neural network to obtain the predicted particle locations. (**D**) The generated particle maps from different sections are then combined to obtain the final 3D segments. (**E**) Explanation of the data fusion strategy, which makes use of the information redundancy of single particle to increase the detection accuracy and segment in 3D without 3D-labeled data.

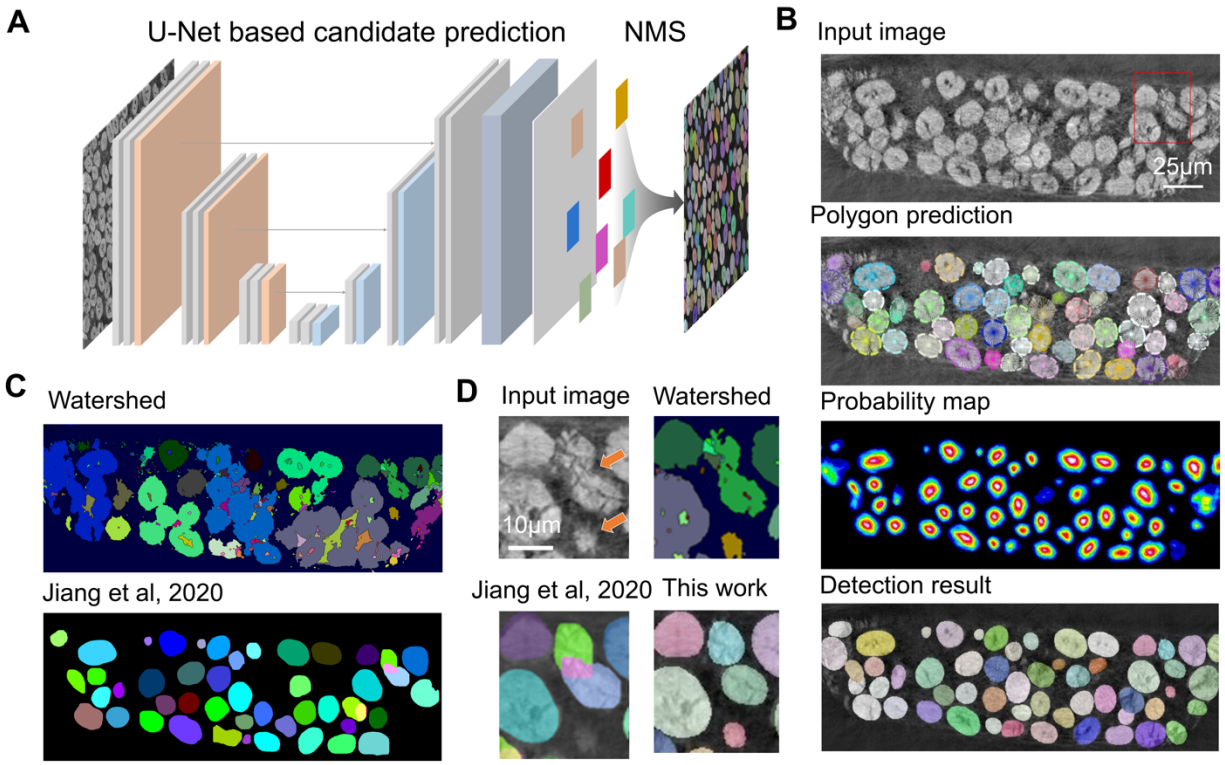

Fig. S3. Details of the morphology-informed neural network and comparison of different particle segmentation methods. (**A**) The particles are densely predicted by a U-Net architecture and then selected the final instances via non-maximum suppression (NMS). (**B**) The network (*47*) predicts the star-convex-polygons constrained particles and the probability map is used to obtain the final detection result. (**C**) The detection results by conventional watershed algorithm and the method in previous publication (*1*). (**D**) Zoomed-in region indicated by red rectangle in (B) to amplify the difference among various methods. Notice the distinguish ability between two particles as indicated by the orange arrow.

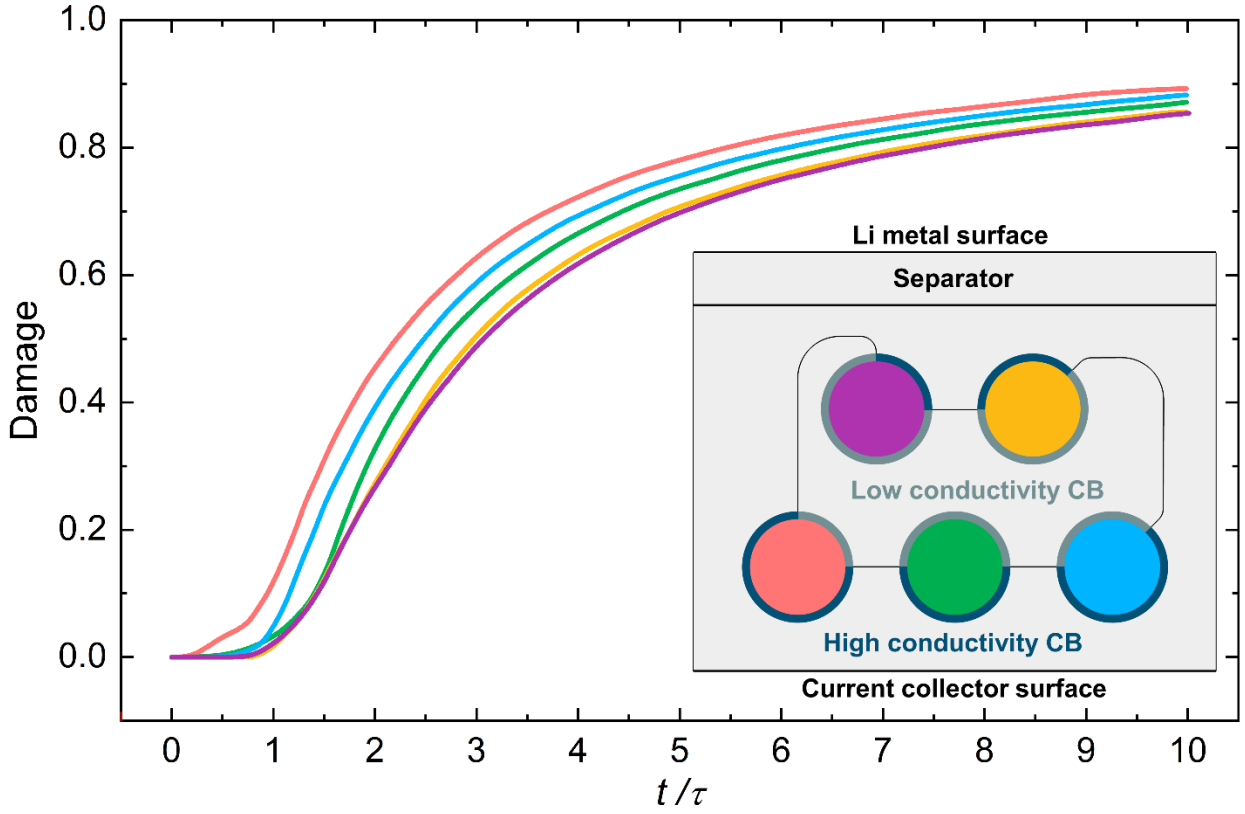

Fig. S4. Additional finite element analysis results of the electrochemical activity and mechanical damage for a half-cell configuration containing five NMC active particles. The inset displays the schematic illustration where two CB domains surround five NMC active particles. The damage profiles follow a pattern similar to the three-particle system with an initial breakout, divergence, and ultimate convergence.

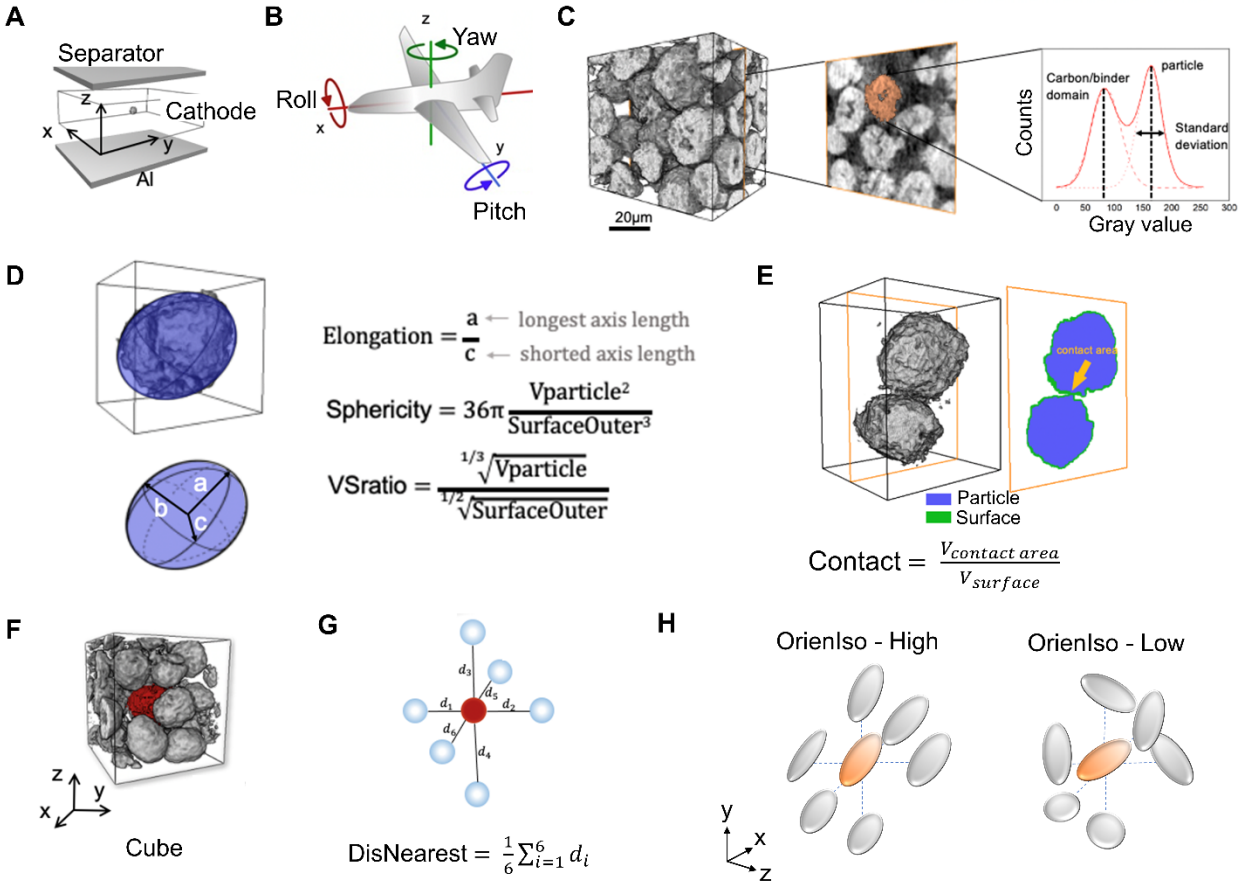

Fig. S5. Graphic illustrations of the typical attributes extracted from the identified NMC particles. The description can be found in Table S1. (**A**) Position, X, Y and Z; (**B**) Position, Yaw, Pitch and Roll; (**C**) The way to determine the electron density and its standard deviation; (**D**) Elongation, sphericity and VSratio; (**E**) Contact; (**F**) Packing density; (**G**) The definition of 6-connectivity of neighbors; (**H**) Orientational isotropy (OrienIso).

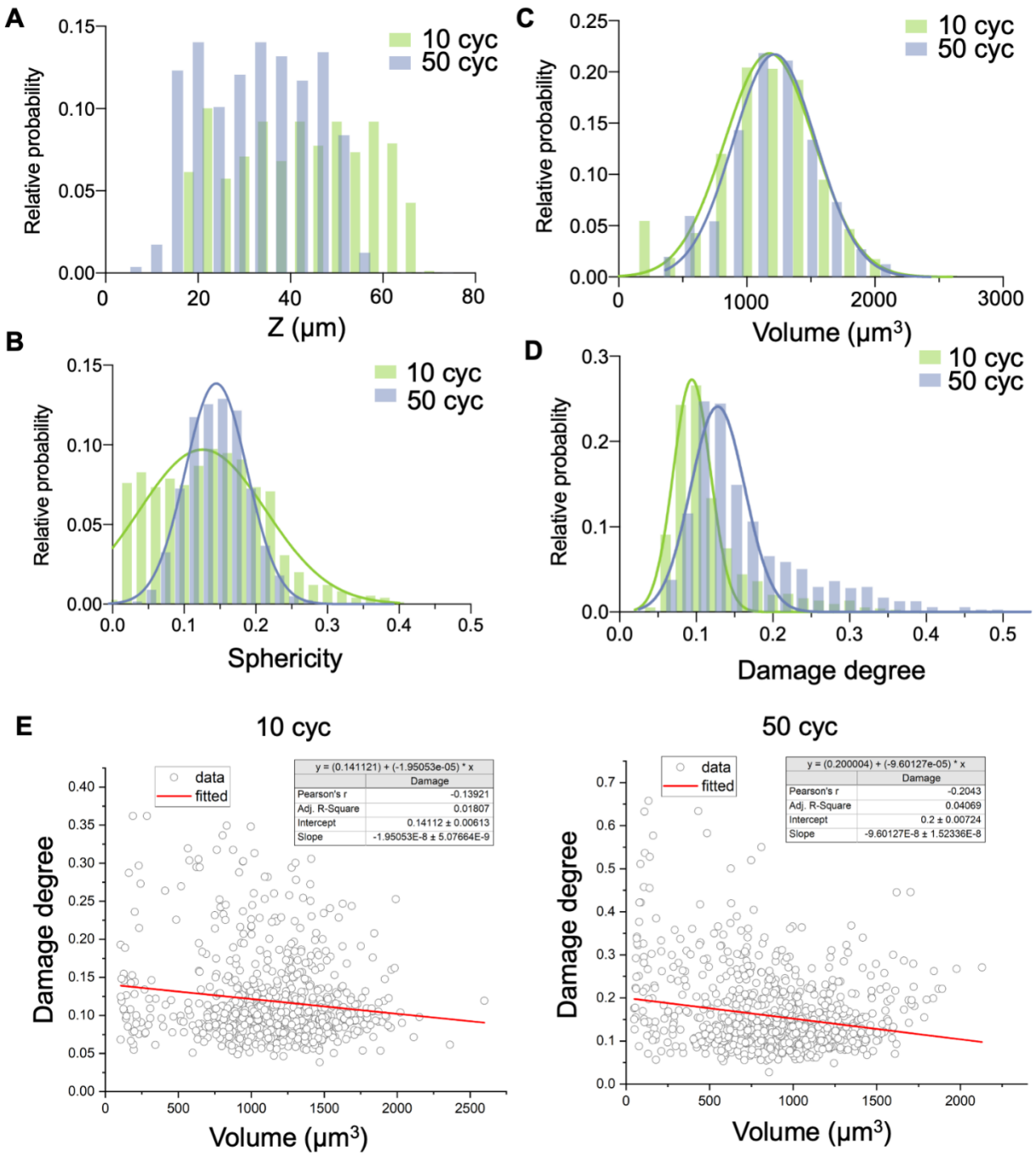

Fig. S6. Statistical comparisons of typical attributes. (**A**) the *z* position, (**B**) sphericity, (**C**) volume and (**D**) the degree of particle damage, are carried out as a function of cycling stages (10 cycles and 50 cycles). (**E**) The plots of damage degree as a function of volume for 10cyc and 50cyc.

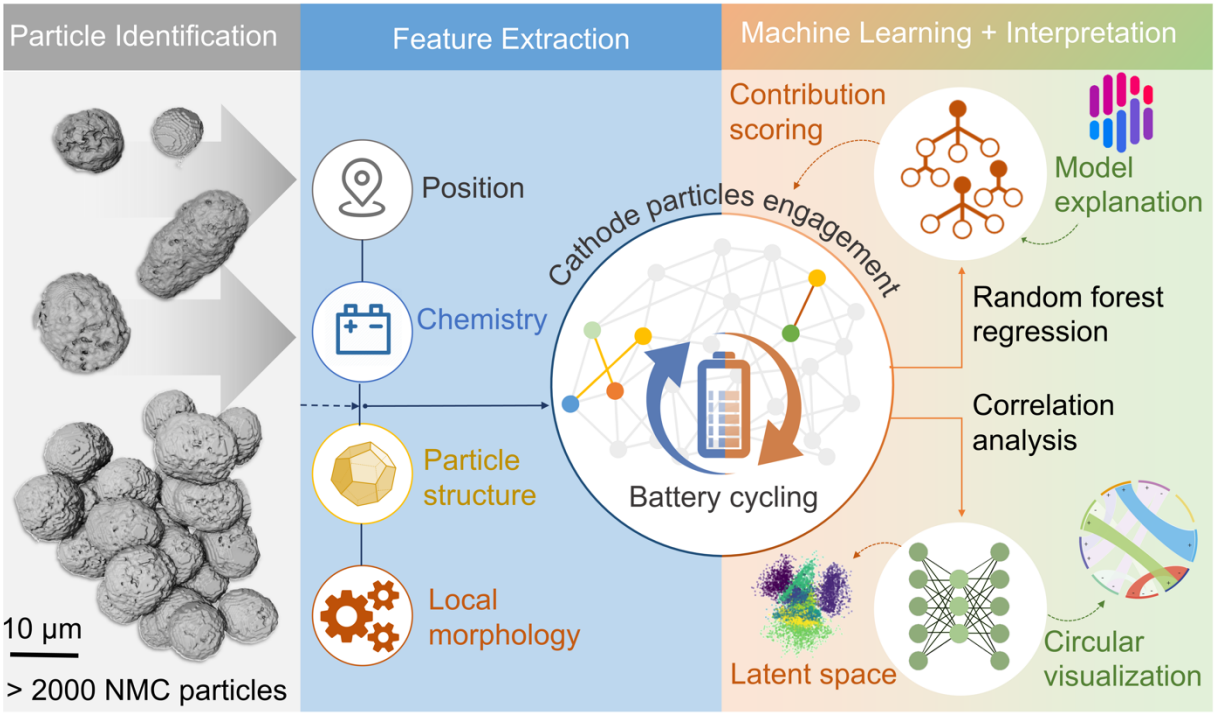

Fig. S7. Illustration of analysis pipeline with the interpretable machine learning framework. Over 2000 NMC cathode particles are firstly identified accurately through morphology-informed neural network. Various particle attributes are then extracted and fed into the interpretable machine learning models to evaluate the correlation between attributes and the scores of each attribute's contribution to the particle damage.

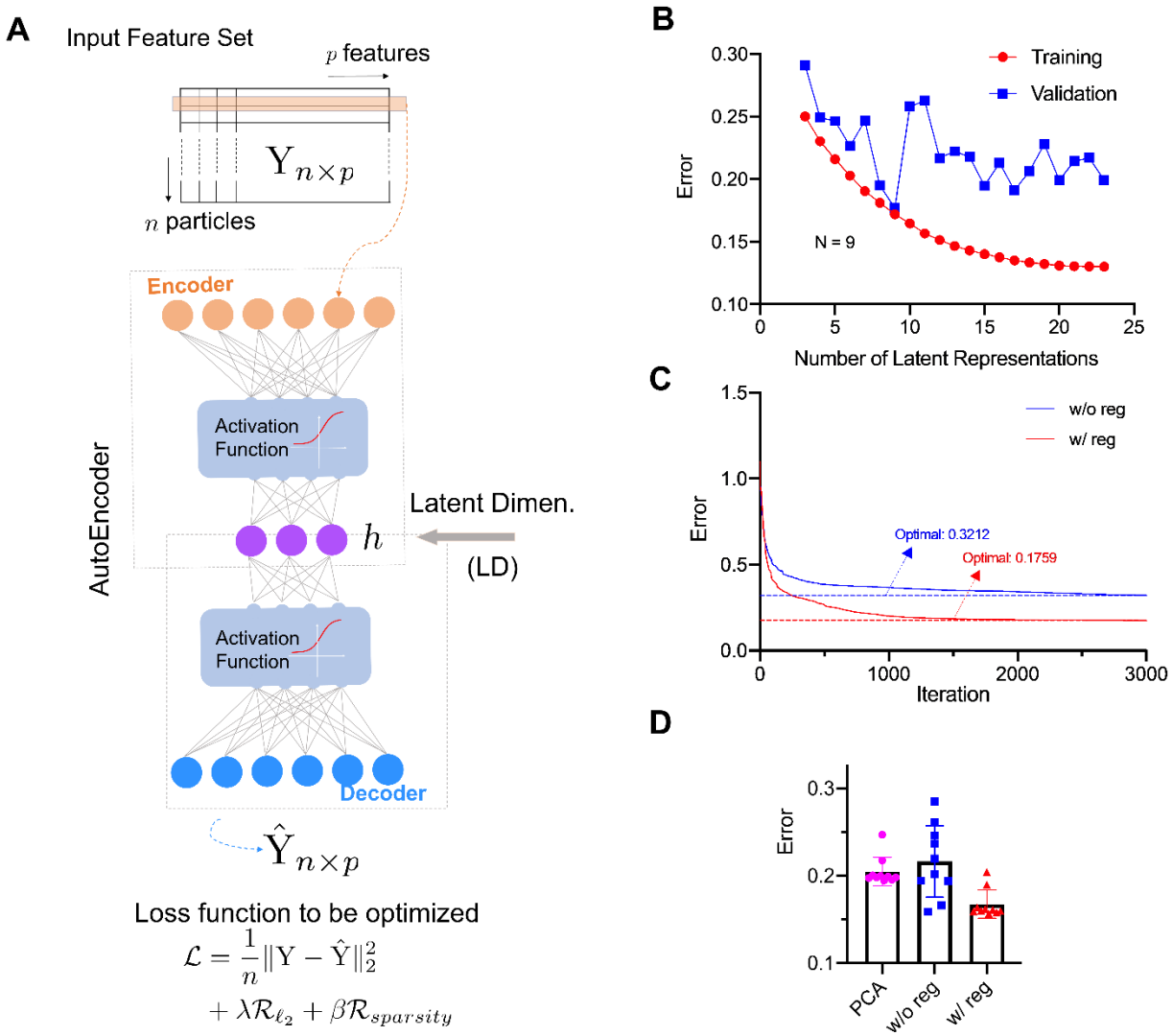

Fig. S8. Regularized auto-encoder network for dimensionality reduction. (**A**) Architecture of the autoencoder neural network. (**B-D**) Evaluation of the proposed autoencoder-based analysis method; (**B**) The optimal number of latent representations is determined by cross-validation. $N = 9$ is chosen to minimize the validation error. (**C**) With the regularization terms, the better performance can be obtained. (**D**) Comparison of the coding-decoding performance between the proposed autoencoder with regularization and the traditional PCA-based method.

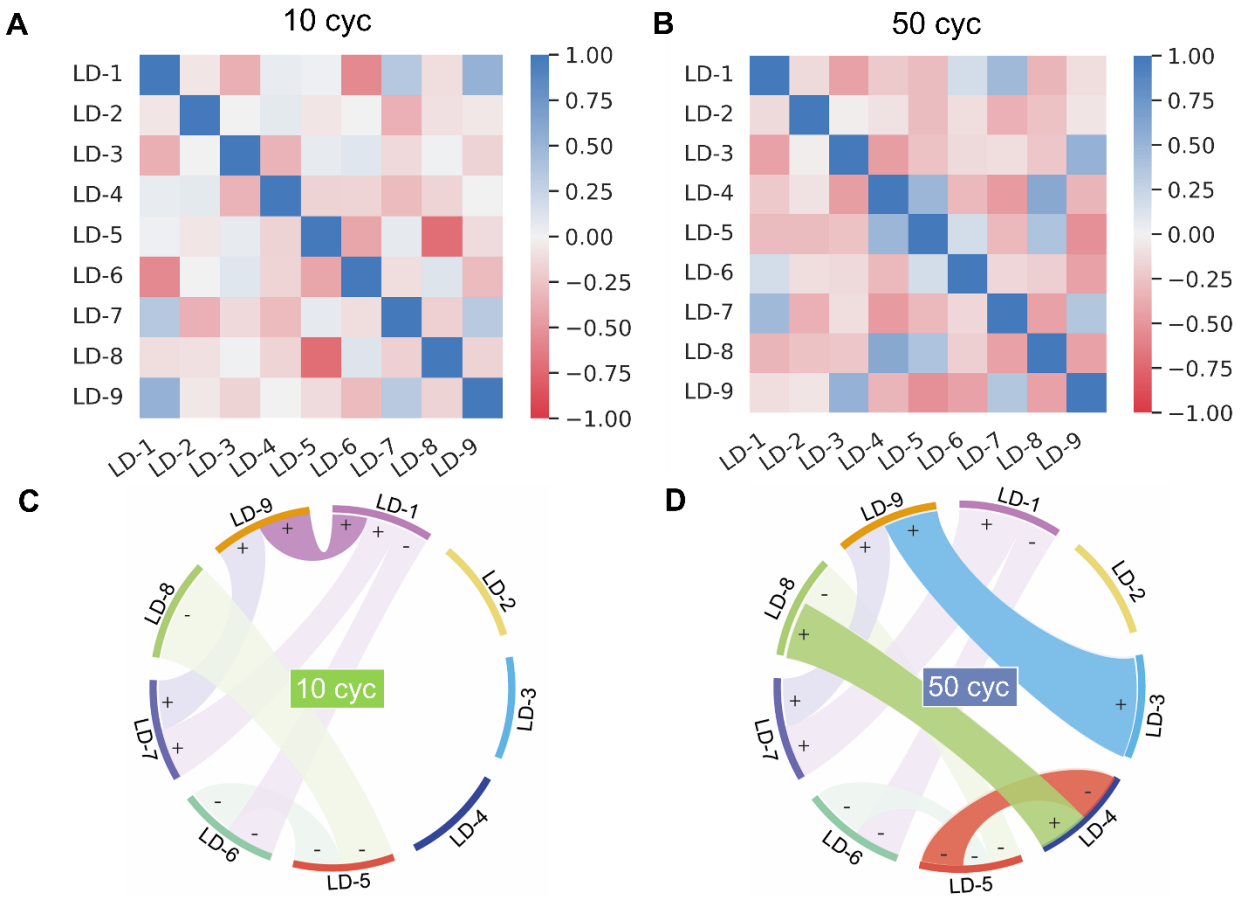

Fig. S9. Correlations between the latent dimensions (LDs). The correlation matrix of 9 LDs in 10-cycled (**A**) and 50-cycled (**B**) electrodes. The corresponding Circular plots of the correlations of 9 LDs in 10-cycled (**C**) and 50-cycled (**D**) electrodes. The "+" and "-" signs denote positive and negative correlation, respectively. The correlations common to both electrodes are set semi-transparent while the different ones are highlighted.

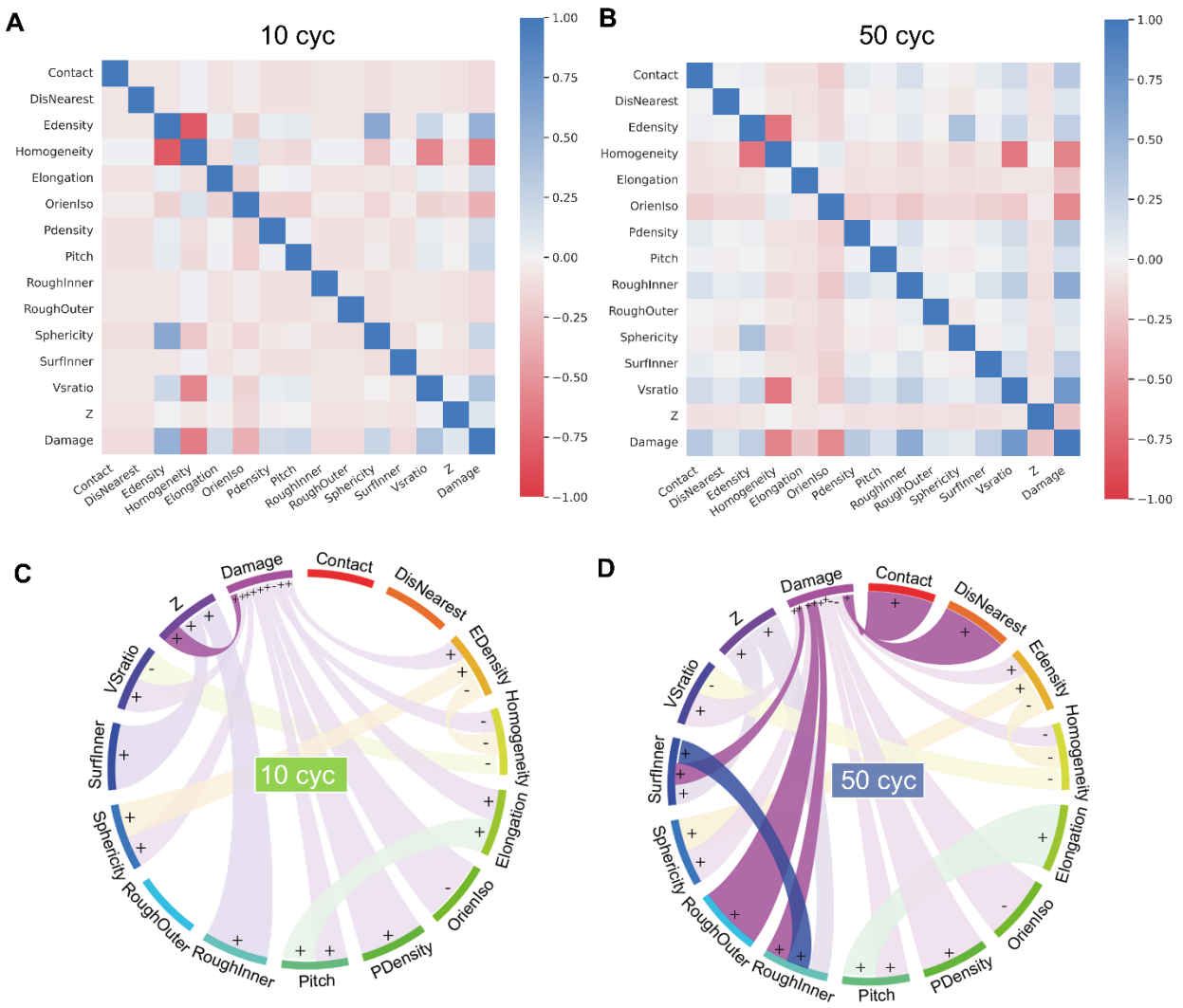

Fig. S10. Correlations between the reconstructed attributes. The correlation matrix of top 15 attributes in 10-cycled (**A**) and 50-cycled (**B**) electrodes. The corresponding Circular plots in the original space in 10-cycled (**C**) and 50-cycled (**D**) electrodes. They are reconstructed from the latent representation through the coding-decoding process by the regularized autoencoder neural network. The common connections are shown in light colors and the different ones are highlighted in dark colors.

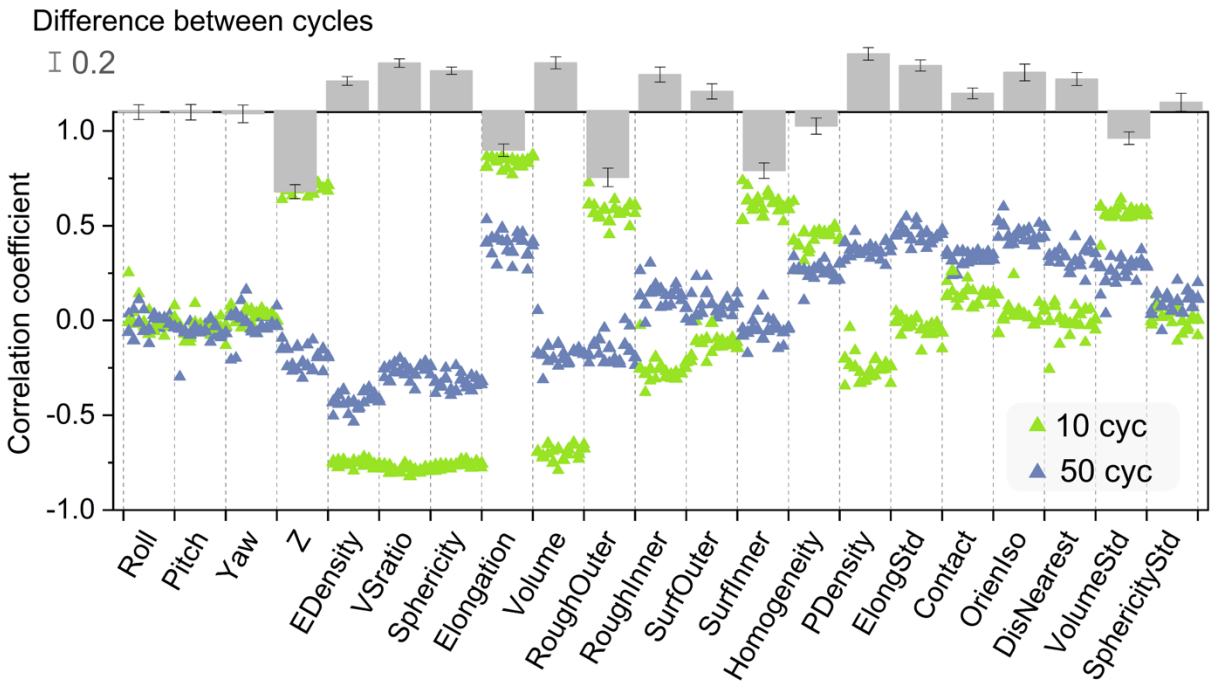

Fig. S11. The Pearson correlation coefficients of all attributes to the particle damage in 10-cycled (green) and 50-cycled (blue) electrodes. Data-subsampling is used for robustness validation. The mean and standard deviation of the differences in the correlation coefficients between the 10-cycled and 50-cycled data are plotted on the top. No obvious transition across cycles is observed by the interpreting method of Pearson correlation coefficients.

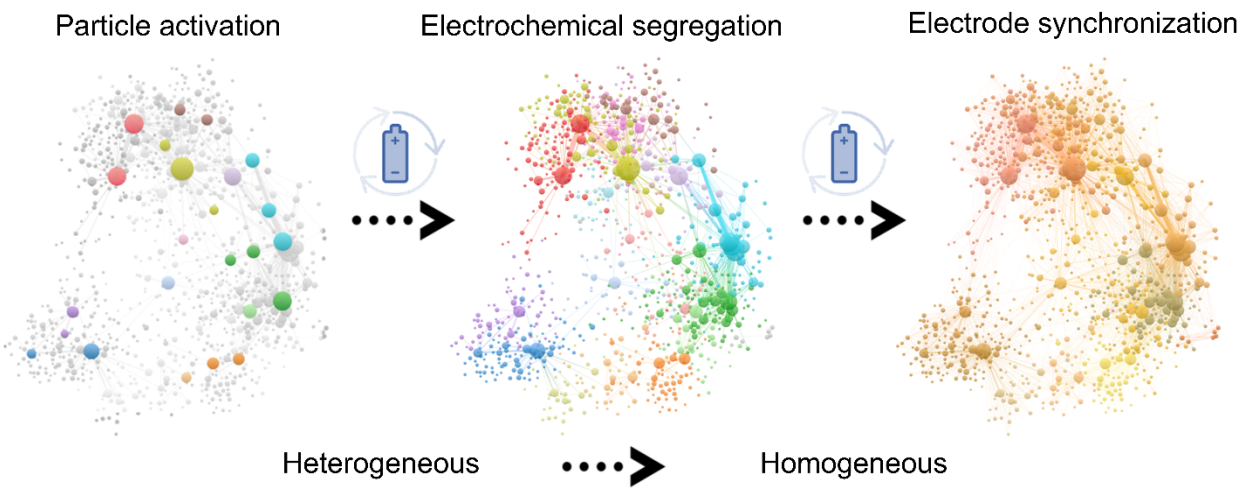

Fig. S12. Schematic illustration of the cathode particle network evolution upon battery cycling. The electrochemical activity and degradation of every single particles co-evolve, causing a transition from particle activation to electrochemical segregation to electrode synchronization. Colors represent different activation states, and the same color indicates that particles are co-evolving.

ID	Name	Description
Group A - Position		
1	X	Particle position in the x axis, see Fig. S5(a).
2	Y	Particle position in the y axis, see Fig. S5(a).
3	Z	Particle position in the z axis, see Fig. S5(a).
4	Yaw	Counterclockwise rotation angle in degrees around the z axis, see Fig. S5(b).
5	Pitch	Counterclockwise rotation angle in degrees around the y axis, see Fig. S5(b).
6	Roll	Counterclockwise rotation angle in degrees around the x axis, see Fig. S5(b).
Group B – Chemical Properties		
7	EDensity	Averaged electron density, which is defined as the averaged values of reconstructed phase map over the entire particle, see Fig. S5(c).
8	Homogeneity	Defined as the inverse of the standard deviation of the phase map over the entire particle, see Fig. S5(c).
Group C – Particle Structure		
9	SurfaceInner	Inner surface area of the particle.
10	SurfaceOuter	Outer surface area of the particle.
11	Volume	Particle volume.
12	Damage	Ratio of the crack volume to the particle volume.
13	Elongation	Ratio of the longest axis length to the shortest axis length, see Fig. S5(d).
14	Sphericity	Ratio of the square volume over the cube of the surface area, normalized such that the value for a ball equals one, see Fig. S5(d).
15	VSratio	The ratio of the cube root of the volume to the square root of the surface, see Fig. S5(d).
16	RoughInner	Roughness of the inner surface.
17	RoughOuter	Roughness of the outer surface.
Group D – Local Morphology		
19	Contact	Ratio of the contact area to the outer surface, see Fig. S5(e).
20	PDensity	Packing density, which is defined as the ratio of the volume of all NMC particles to the volume of the cube (100 x 100 x 100 μm), see Fig. S5(f).
21	DistNearest	Averaged distance to the nearest particles considering the 6-connectivity, see Fig. S5(g).
22	ElongStd	Standard deviation of the elongation over the six nearest particles.
23	VolumeStd	Standard deviation of the volume over the six nearest particles.
24	OrienIso	Orientational isotropy, the degree of orientational alignment for the six nearest particles, see Fig. S5(h).

Table S1. Name and description of all extracted attribute from the identified NMC particles. They are grouped into four categories: position, chemistry, particle structure and local morphology. The corresponding graphic illustrations can be found in **Fig. S5**.

References and Notes

1. Z. Jiang, J. Li, Y. Yang, L. Mu, C. Wei, X. Yu, P. Pianetta, K. Zhao, P. Cloetens, F. Lin, Y. Liu, Machine-learning-revealed statistics of the particle-carbon/binder detachment in lithium-ion battery cathodes. *Nat. Commun.* **11**, 2310 (2020). doi:10.1038/s41467-020-16233-5 Medline

2. D. E. Stephenson, B. C. Walker, C. B. Skelton, E. P. Gorzkowski, D. J. Rowenhorst, D. R. Wheeler, Modeling 3D microstructure and ion transport in porous Li-ion battery electrodes. *J. Electrochem. Soc.* **158**, A781 (2011). doi:10.1149/1.3579996

3. R. Xu, Y. Yang, F. Yin, P. Liu, P. Cloetens, Y. Liu, F. Lin, K. Zhao, Heterogeneous damage in Li-ion batteries: Experimental analysis and theoretical modeling. *J. Mech. Phys. Solids* **129**, 160–183 (2019). doi:10.1016/j.jmps.2019.05.003

4. Z. Xu, M. M. Rahman, L. Mu, Y. Liu, F. Lin, Chemomechanical behaviors of layered cathode materials in alkali metal ion batteries. *J. Mater. Chem. A* **6**, 21859–21884 (2018). doi:10.1039/C8TA06875E

5. L. Mu, R. Lin, R. Xu, L. Han, S. Xia, D. Sokaras, J. D. Steiner, T.-C. Weng, D. Nordlund, M. M. Doeff, Y. Liu, K. Zhao, H. L. Xin, F. Lin, Oxygen release induced chemomechanical breakdown of layered cathode materials. *Nano Lett.* **18**, 3241–3249 (2018). doi:10.1021/acs.nanolett.8b01036 Medline

6. Z. Yang, F. Lin, Heterogeneous, defect-rich battery particles and electrodes: Why do they matter, and how can one leverage them? *J. Phys. Chem. C* **125**, 9618–9629 (2021). doi:10.1021/acs.jpcc.1c01703

7. H. Liu, M. Wolf, K. Karki, Y.-S. Yu, E. A. Stach, J. Cabana, K. W. Chapman, P. J. Chupas, Intergranular cracking as a major cause of long-term capacity fading of layered cathodes. *Nano Lett.* **17**, 3452–3457 (2017). doi:10.1021/acs.nanolett.7b00379 Medline

8. Y. Mao, X. Wang, S. Xia, K. Zhang, C. Wei, S. Bak, Z. Shadike, X. Liu, Y. Yang, R. Xu, P. Pianetta, S. Ermon, E. Stavitski, K. Zhao, Z. Xu, F. Lin, X. Yang, E. Hu, Y. Liu, High-voltage charging-induced strain, heterogeneity, and micro-cracks in secondary particles of a nickel-rich layered cathode material. *Adv. Funct. Mater.* **29**, 1900247 (2019). doi:10.1002/adfm.201900247

9. F. Lin, K. Zhao, Y. Liu, Heterogeneous reaction activities and statistical characteristics of particle cracking in battery electrodes. *ACS Energy Lett.* **6**, 4065–4070 (2021). doi:10.1021/acsenergylett.1c02135

10. H. H. Sun, H.-H. Ryu, U.-H. Kim, J. A. Weeks, A. Heller, Y.-K. Sun, C. B. Mullins, Beyond doping and coating: Prospective strategies for stable high-capacity layered Ni-rich cathodes. *ACS Energy Lett.* **5**, 1136–1146 (2020). doi:10.1021/acsenergylett.0c00191

11. W. E. Gent, Y. Li, S. Ahn, J. Lim, Y. Liu, A. M. Wise, C. B. Gopal, D. N. Mueller, R. Davis, J. N. Weker, J. H. Park, S. K. Doo, W. C. Chueh, Persistent state-of-charge heterogeneity in relaxed, partially charged $Li_{1-x}Ni_{1/3}Co_{1/3}Mn_1/3O_2$ secondary particles. *Adv. Mater.* **28**, 6631–6638 (2016). doi:10.1002/adma.201601273 Medline

12. X. Lu, A. Bertei, D. P. Finegan, C. Tan, S. R. Daemi, J. S. Weaving, K. B. O'Regan, T. M. M. Heenan, G. Hinds, E. Kendrick, D. J. L. Brett, P. R. Shearing, 3D microstructure design of lithium-ion battery electrodes assisted by X-ray nano-computed tomography

and modelling. *Nat. Commun.* **11**, 2079 (2020). doi:10.1038/s41467-020-15811-x Medline

13. X. Liu, B. Zheng, J. Zhao, W. Zhao, Z. Liang, Y. Su, C. Xie, K. Zhou, Y. Xiang, J. Zhu, H. Wang, G. Zhong, Z. Gong, J. Huang, Y. Yang, Electrochemo-mechanical effects on structural integrity of Ni-rich cathodes with different microstructures in all solid-state batteries. *Adv. Energy Mater.* **11**, 2003583 (2021). doi:10.1002/aenm.202003583

14. W. Li, E. M. Erickson, A. Manthiram, High-nickel layered oxide cathodes for lithium-based automotive batteries. *Nat. Energy* **5**, 26–34 (2020). doi:10.1038/s41560-019-0513-0

15. Z. Xu, Z. Jiang, C. Kuai, R. Xu, C. Qin, Y. Zhang, M. M. Rahman, C. Wei, D. Nordlund, C.-J. Sun, X. Xiao, X.-W. Du, K. Zhao, P. Yan, Y. Liu, F. Lin, Charge distribution guided by grain crystallographic orientations in polycrystalline battery materials. *Nat. Commun.* **11**, 83 (2020). doi:10.1038/s41467-019-13884-x Medline

16. A. Liu, N. Zhang, J. E. Stark, P. Arab, H. Li, J. R. Dahn, Synthesis of Co-free Ni-rich single crystal positive electrode materials for lithium ion batteries: Part II. One-step lithiation method of Mg-doped $LiNiO_2$. *J. Electrochem. Soc.* **168**, 050506 (2021). doi:10.1149/1945-7111/abf9c2

17. A. J. Merryweather, C. Schnedermann, Q. Jacquet, C. P. Grey, A. Rao, Operando optical tracking of single-particle ion dynamics in batteries. *Nature* **594**, 522–528 (2021). doi:10.1038/s41586-021-03584-2 Medline

18. S. Kuppan, Y. Xu, Y. Liu, G. Chen, Phase transformation mechanism in lithium manganese nickel oxide revealed by single-crystal hard X-ray microscopy. *Nat. Commun.* **8**, 14309 (2017). doi:10.1038/ncomms14309 Medline

19. M. Yoon, Y. Dong, J. Hwang, J. Sung, H. Cha, K. Ahn, Y. Huang, S. J. Kang, J. Li, J. Cho, Reactive boride infusion stabilizes Ni-rich cathodes for lithium-ion batteries. *Nat. Energy* **6**, 362–371 (2021). doi:10.1038/s41560-021-00782-0

20. J.-N. Zhang, Q. Li, C. Ouyang, X. Yu, M. Ge, X. Huang, E. Hu, C. Ma, S. Li, R. Xiao, W. Yang, Y. Chu, Y. Liu, H. Yu, X.-Q. Yang, X. Huang, L. Chen, H. Li, Trace doping of multiple elements enables stable battery cycling of $LiCoO_2$ at 4.6 V. *Nat. Energy* **4**, 594–603 (2019). doi:10.1038/s41560-019-0409-z

21. Y.-K. Sun, S.-T. Myung, B.-C. Park, J. Prakash, I. Belharouak, K. Amine, High-energy cathode material for long-life and safe lithium batteries. *Nat. Mater.* **8**, 320–324 (2009). doi:10.1038/nmat2418 Medline

22. F. Lin, D. Nordlund, Y. Li, M. K. Quan, L. Cheng, T.-C. Weng, Y. Liu, H. L. Xin, M. M. Doeff, Metal segregation in hierarchically structured cathode materials for high-energy lithium batteries. *Nat. Energy* **1**, 15004 (2016). doi:10.1038/nenergy.2015.4

23. Z. Zhu, D. Yu, Y. Yang, C. Su, Y. Huang, Y. Dong, I. Waluyo, B. Wang, A. Hunt, X. Yao, J. Lee, W. Xue, J. Li, Gradient Li-rich oxide cathode particles immunized against oxygen release by a molten salt treatment. *Nat. Energy* **4**, 1049–1058 (2019). doi:10.1038/s41560-019-0508-x

24. H. H. Sun, U.-H. Kim, J.-H. Park, S.-W. Park, D.-H. Seo, A. Heller, C. B. Mullins, C. S. Yoon, Y.-K. Sun, Transition metal-doped Ni-rich layered cathode materials for durable

Li-ion batteries. *Nat. Commun.* **12**, 6552 (2021). doi:10.1038/s41467-021-26815-6 Medline

25. C. Delacourt, P. Poizot, S. Levasseur, C. Masquelier, Size effects on carbon-free $LiFePO_4$ powders. *Electrochem. Solid-State Lett.* **9**, A352 (2006). doi:10.1149/1.2201987

26. L. Bläubaum, F. Röder, C. Nowak, H. S. Chan, A. Kwade, U. Krewer, Impact of particle size distribution on performance of lithium-ion batteries. *ChemElectroChem* **7**, 4755–4766 (2020). doi:10.1002/celc.202001249

27. D.-H. Kim, J. Kim, Synthesis of $LiFePO_4$ nanoparticles and their electrochemical properties. *J. Phys. Chem. Solids* **68**, 734–737 (2007). doi:10.1016/j.jpcs.2007.03.019

28. Y. Yang, R. Xu, K. Zhang, S. Lee, L. Mu, P. Liu, C. K. Waters, S. Spence, Z. Xu, C. Wei, D. J. Kautz, Q. Yuan, Y. Dong, Y. Yu, X. Xiao, H. Lee, P. Pianetta, P. Cloetens, J. Lee, K. Zhao, F. Lin, Y. Liu, Quantification of heterogeneous degradation in Li-ion batteries. *Adv. Energy Mater.* **9**, 1900674 (2019). doi:10.1002/aenm.201900674

29. J. Park, H. Zhao, S. D. Kang, K. Lim, C.-C. Chen, Y.-S. Yu, R. D. Braatz, D. A. Shapiro, J. Hong, M. F. Toney, M. Z. Bazant, W. C. Chueh, Fictitious phase separation in Li layered oxides driven by electro-autocatalysis. *Nat. Mater.* **20**, 991–999 (2021). doi:10.1038/s41563-021-00936-1 Medline

30. J. Li, Z. Zhou, Z. Luo, Z. He, J. Zheng, Y. Li, J. Mao, K. Dai, Microcrack generation and modification of Ni-rich cathodes for Li-ion batteries: A review. *Sustain Mater Technologies.* **29**, e00305 (2021). doi:10.1016/j.susmat.2021.e00305

31. M. A. Kramer, Nonlinear principal component analysis using autoassociative neural networks. *AIChE J.* **37**, 233–243 (1991). doi:10.1002/aic.690370209

32. L. Breiman, Random forests. *Mach. Learn.* **45**, 5–32 (2001). doi:10.1023/A:1010933404324

33. S. M. Lundberg, G. Erion, H. Chen, A. DeGrave, J. M. Prutkin, B. Nair, R. Katz, J. Himmelfarb, N. Bansal, S.-I. Lee, From local explanations to global understanding with explainable AI for trees. *Nat. Mach. Intell.* **2**, 56–67 (2020). doi:10.1038/s42256-019-0138-9 Medline

34. M. Krzywinski, J. Schein, I. Birol, J. Connors, R. Gascoyne, D. Horsman, S. J. Jones, M. A. Marra, Circos: An information aesthetic for comparative genomics. *Genome Res.* **19**, 1639–1645 (2009). doi:10.1101/gr.092759.109 Medline

35. R. Gómez-Bombarelli, J. N. Wei, D. Duvenaud, J. M. Hernández-Lobato, B. Sánchez-Lengeling, D. Sheberla, J. Aguilera-Iparraguirre, T. D. Hirzel, R. P. Adams, A. Aspuru-Guzik, Automatic chemical design using a data-driven continuous representation of molecules. *ACS Cent. Sci.* **4**, 268–276 (2018). doi:10.1021/acscentsci.7b00572 Medline

36. G. Qian, J. Zhang, S.-Q. Chu, J. Li, K. Zhang, Q. Yuan, Z.-F. Ma, P. Pianetta, L. Li, K. Jung, Y. Liu, Understanding the mesoscale degradation in nickel-rich cathode materials through machine-learning-revealed strain–redox decoupling. *ACS Energy Lett.* **6**, 687–693 (2021). doi:10.1021/acsenergylett.0c02699

37. L. S. Shapley, "A value for n-person games" (RAND Corporation, 1953); https://www.rand.org/pubs/papers/P295.html.

38. S. Lundberg, S.-I. Lee, A unified approach to interpreting model predictions arXiv:1705.07874 [cs.AI] (2017).

39. J. Hu, B. Wu, X. Cao, Y. Bi, S. Chae, C. Niu, B. Xiao, J. Tao, J. Zhang, J. Xiao, Evolution of the rate-limiting step: From thin film to thick Ni-rich cathodes. *J. Power Sources* **454**, 227966 (2020). doi:10.1016/j.jpowsour.2020.227966

40. J. Billaud, F. Bouville, T. Magrini, C. Villevieille, A. R. Studart, Magnetically aligned graphite electrodes for high-rate performance Li-ion batteries. *Nat. Energy* **1**, 16097 (2016). doi:10.1038/nenergy.2016.97

41. J. S. Sander, R. M. Erb, L. Li, A. Gurijala, Y.-M. Chiang, High-performance battery electrodes via magnetic templating. *Nat. Energy* **1**, 16099 (2016). doi:10.1038/nenergy.2016.99

42. C. Lei, Z. Xie, K. Wu, Q. Fu, Controlled vertically aligned structures in polymer composites: Natural inspiration, structural processing, and functional application. *Adv. Mater.* **33**, e2103495 (2021). doi:10.1002/adma.202103495 Medline

43. J. Li, N. Sharma, Z. Jiang, Y. Yang, F. Monaco, Z. Xu, D. Hou, D. Ratner, P. Pianetta, P. Cloetens, F. Lin, K. Zhao, Y. Liu, Data for: Dynamics of particle network in composite battery cathodes, Zenodo (2022); https://doi.org/10.5281/zenodo.5888945.

44. J. C. da Silva, A. Pacureanu, Y. Yang, S. Bohic, C. Morawe, R. Barrett, P. Cloetens, Efficient concentration of high-energy x-rays for diffraction-limited imaging resolution. *Optica* **4**, 492 (2017). doi:10.1364/OPTICA.4.000492

45. P. Cloetens, W. Ludwig, J. Baruchel, D. Van Dyck, J. Van Landuyt, J. P. Guigay, M. Schlenker, Holotomography: Quantitative phase tomography with micrometer resolution using hard synchrotron radiation x rays. *Appl. Phys. Lett.* **75**, 2912–2914 (1999). doi:10.1063/1.125225

46. A. Mirone, E. Brun, E. Gouillart, P. Tafforeau, J. Kieffer, The PyHST2 hybrid distributed code for high speed tomographic reconstruction with iterative reconstruction and a priori knowledge capabilities. *Nucl. Instrum. Methods Phys. Res. B* **324**, 41–48 (2014). doi:10.1016/j.nimb.2013.09.030

47. U. Schmidt, M. Weigert, C. Broaddus, G. Myers, "Cell detection with star-convex polygons," in *International Conference on Medical Image Computing and Computer-Assisted Intervention*, A. Frangi, J. Schnabel, C. Davatzikos, C. Alberola-López, G. Fichtinger, Eds. (Springer, 2018), vol. 11071, pp. 265–273.

48. O. Ronneberger, P. Fischer, T. Brox, "U-Net: Convolutional networks for biomedical image segmentation," in *Medical Image Computing and Computer-Assisted Intervention – MICCAI 2015*, N. Navab, J. Hornegger, W. Wells, A. Frangi, Eds. (Springer, 2015), pp. 234–241.